Comparison of machining performance of stainless steel 316L produced by selective laser melting and electron beam melting

Available online at www.sciencedirect.com

ScienceDirect

Procedia CIRP 115 (2022) 72–77

www.elsevier.com/locate/procedia

10th CIRP Global Web Conference – Material Aspects of Manufacturing Processes

Comparison of machining performance of stainless steel 316L produced by selective laser melting and electron beam melting

S. B. Hosseini[a, b, *], D. Mallipeddi[b], J. Holmberg[a], L.-E. Rännar[c], A. Koptyug[c], W. Sjöström[c], P. Krajnik[b], U. Klement[b]

[a]*Department of Manufacturing Processes, Research Institutes of Sweden AB (RISE AB), Argongatan 30, 431 53 Mölndal, Sweden*
[b]*Department of Industrial and Materials Science, Chalmers University of Technology, Gothenburg 41296, Sweden*
[c]*Mid Sweden University, Sports Tech Research Centre, Akademigatan 1, SE-83125, Östersund, Sweden*

* Corresponding author. Tel.: +46(0)707-80 6169. *E-mail address: seyed.hosseini@ri.se*

Abstract

Powder bed fusion processes based additively manufactured SS 316L components fall short of surface integrity requirements needed for optimal functional performance. Hence, machining is required to achieve dimensional accuracy and to enhance surface integrity characteristics. This research is focused on comparing the material removal performance of 316L produced by PBF-LB (laser) and PBF-EB (electron beam) in terms of tool wear and surface integrity. The results showed comparable surface topography and residual stress profiles. While the hardness profiles revealed work hardening at the surface where PBF-LB specimens being more susceptible to work hardening. The investigation also revealed differences in the progress of the tool wear when machining specimens produced with either PBF-LB or PBF-EB.

Keywords: Additive manufacturing; machining; surface integrity; selective laser melting; electron beam melting

1. Introduction

Additive manufacturing (AM) enables manufacturing of complex parts directly from the 3D-CAD design without the need of expensive tooling [1]. AM is today used in various sectors such as aerospace [2], tooling [3], and energy [4]. Powder bed fusion (PBF) processes using either laser (PBF-LB) or electron beam (PBF-EB) as energy source are the most widely used/accepted technologies in the industry. These methods have shown promising results in producing dense parts with high accuracy, reproducibility, and good mechanical and thermal properties [5-8]. Among steels, much attention has been paid to 316L austenitic stainless steel since it is widely used for different commercial applications due to its superior mechanical properties, excellent corrosion and oxidation resistance [5]. Despite significant process optimization efforts, 316L parts manufactured by PBF-LB and PBF-EB still do not meet the surface quality requirements needed for optimal functional performance. Typical surface roughness (Ra) values for 316L parts produced by PBF-LB and PBF-EB have been reported to be ~10 µm [9] and ~30 µm [10], respectively. The large difference in the surface roughness as obtained above between PBF-LB and PBF-EB is material independent. Comparable surface roughness values have been reported for Ti6Al4V when comparing PBF-LB and PBF-EB. For the PBF-LB specimens, Ra of ~8 µm was measured in the build direction, whereas for the PBF-EB, Ra of ~23 µm was observed [11]. Regardless of the concerned AM-process, printed parts typically require post-processing to achieve the desired surface

10.1016/j.procir.2022.10.052

quality required for functional components. When studying the effect of turning, drag finish and vibratory surface finishing on 316L produced by PBF-LB, it was found that turning results in the best surface roughness, ~2 µm [12]. Besides surface roughness, sub-surface defects such as pores have a strong influence on the mechanical properties and must therefore be considered. They can be categorized into i) functional pores, ii) microstructural pores, and iii) structural pores [13]. The functional and microstructural pores are undesirable and there is a need to eliminate them or minimize their presence for enhanced performance. This was shown when studying the fatigue strength of AM in comparison to wrought stainless 316L [7]. The fatigue strength of the specimens produced with PBF-LB was significantly lower in the as-printed condition compared to the wrought ones. However, upon machining (turning), the PBF-LB specimens outperformed their wrought counterparts. The enhanced fatigue strength was attributed to the elimination of surface pores located between the outer contour and hatch region. Moreover, the printing strategy also plays a crucial role in defining the surface integrity, i.e. printing with or without contour strategy. For Ti6Al4V when printing without any contour when printing with PBF-EB, the depth of cut (a_p) should be >1 mm to avoid the near surface pores and thus improve the surface quality [14]. However, when applying three or five contours, a_p of 0.25 mm was enough to avoid surface and near surface defects. Despite the extensive research in AM, knowledge of the machinability of AM materials is limited, which hinders a faster adoption of AM. Clearly, optimization of both the printing and post- processing is needed for achieving long service life and best surface quality at minimum cost. The research presented here focused on comparing the surface integrity such as surface topography, residual stresses, surface deformation, and hardness for specimens produced with PBF-LB and PBF-EB.

2. Experimental procedure

2.1 Precursor powders

The material for the PBF-EB process was a gas-atomized 316L stainless steel powder with nearly spherical particles ranging in size from 53 to 150 µm (Carpenter powder products AB, Torshälla, Sweden). The powder used for this study was recycled and was previously reported in Ref. [6]. The precursor material for the PBF-LB process was gas-atomized SS316L powder with nearly spherical particles ranging in size from 15 to 45 µm (HC Starck). In case of the PBF-LB process (according to the recommendation from the machine manufacturer), the powder was dried at 60 °C for 24 h and sieved prior to loading into the machine. The chemical composition of the powders used for both processes is given in Table 1.

Table 1. Chemical composition of the precursor powders. All values are given in wt.% unless another unit is given.

Element	Cr	Ni	Mo	Mn	Si	C	Fe	O
PBF-EB	17.6	12.3	2.46	1.7	0.5	0.013	Bal.	145 ppm
PBF-LB	17.8	13.8	2.7	1.5	<0.1	-	Bal.	

2.2 Additive manufacturing

The SLM 125 HL system that was used for the PBF-LB specimens, was equipped with a 400 W YAG-fiber laser (spot size 65 µm). During printing using the stripe pattern, the build plate was heated to 100 °C, and argon 4.8 was used as protective atmosphere. In each layer, first the contour was printed followed by the core. The contour pattern consists of two borders (contours) and one fill contour. The laser power was 200 W, scan speed 800 mm/s, layer thickness was set to 30 µm, and hatch distance 120 µm. The Arcam A2 machine with a 3kW tungsten filament-based electron gun was used to produce the PBF-EB specimens. Initially, a stainless-steel start plate with the dimensions 150 × 150 × 10 mm^3 was heated up to 820 °C, after which the printing operation was started. The layer thickness was set to 70 µm and the time used for consolidating each layer was between 80 and 100 s. Layer melting was using three contours and a raster type hatch for the bulk section. The offset between outer contour and middle contour was 0.3 mm, between middle and inner one- 0.25 mm, and between inner contour and hatch/bulk- 0.05 mm. The snake pattern hatch with a line offset of 0.2 mm and a 90° change in hatching direction in each consecutive layer was used. The dimension of the tubular test samples was: length (L) 110 mm, outer diameter (OD) 55 mm, and wall thickness (t) of 17.5 mm.

2.3 Machining

The turning tests were performed in an EMCO 365 CNC lathe equipped with a Kistler 9275A three-component dynamometer. As cutting inserts, the carbide inserts (DNMG150404SF1125) from Sandvik Coromant was used together with the tool holder DCGNL 16 4D (Sandvik Coromant). The cutting fluid (6-7% emulsion) was applied to the rake face of the insert. The cutting speeds (V_c) 130, 180 and 230 m/min were studied, and the depth of cut (a_p) and feed rate (f) were kept constant at 0.25 mm and 0.15 mm, respectively. In Step 1, the specimen was clamped at the center, after which one side was machined in a stepwise approach starting with CL50 (cutting length 50 mm) according to Fig. 1a. In Step 2, the specimen was once again clamped at the center, after which the stepwise machining procedure was applied on the other half of the specimen (Fig. 1b).

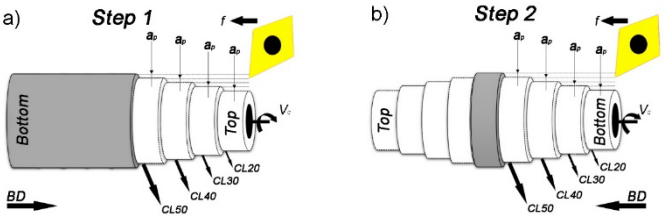

Fig. 1. Schematic illustration of the turning procedure of the samples. The CL50, CL40, CL30 and CL20 corresponds to the cutting lengths of 50mm, 40mm, 30mm and 20mm, respectively.

2.4 Characterization

To differentiate the section of the sample closest to the build platform from the top one, we hereafter refer to Top (upper part of the specimens) and Bottom (lower part of the specimens). Residual stress measurements were performed with X-ray diffraction using a Stresstech G2R XStress 3000 diffractometer

equipped with a Mn X-ray tube (λ: 0.21031 nm). The modified $\sin^2\chi$ method was used with ±5 tilt (psi) angles (from 40° to -40°) and the 152.3° diffraction peak corresponding to the (311) diffraction planes. All measurements were performed in an accredited laboratory in accordance with the EN 15305:2008 standard [15]. Surface topography was measured by Coherence Scanning Interferometry with a Sensofar S Neox instrument. The measurements were performed over a 7.0 mm × 1.3 mm surface constructed of 5 stitched measurement sections to fulfill requirements of EN ISO 4287 [16]. The topography was evaluated according to ISO 25178-2:2012 standard [17]. The hardness of the as printed and machined samples was evaluated using Knoop and Vickers indents at low loads (10-50 g). The hardness of both the as-printed and machined samples was measured from the outer surface to the center of the sample. For the microstructure evaluation, machined samples were cut and prepared following Struers recommendations for stainless steel. The microstructure was revealed using electro-chemical etching in a water-based 10% oxalic acid solution with 3V and 1V potential for PBF-LB and PBF-EB samples, respectively. To investigate whether the machining process affected the surfaces, the microstructure was examined using both the Zeiss Discovery V20 Stereo-light optical microscope and the LEO 1550 Gemini scanning electron microscope (SEM). The progression of the tool wear during the tests was followed by a light optical microscopy. After the tests, the worn inserts were characterized by SEM before and after removing the adhered layer. The adhered layer was removed in diluted HCl.

3. Results and discussion

3.1 *Effect of machining on near surface microstructure and hardness*

Fig. 2 shows the polished and etched sample cut parallel to the build direction (BD), revealing the boundaries of the melt pools in the PBF-LB (Fig. 2a) and PBF-EB (Fig. 2b) specimens. Fig. 2c-d illustrate the layout of periphery sections with the three and four contour lines. The width of the melt traces of the contours in PBF-LB and PBF-EB is ~90 µm, and ~200 µm, respectively. Hence, in the first cutting pass of the PBF-LB samples, both the 1st and 2nd contour and a part of the filling contour is removed. This can be compared to the PBF-EB specimens, where the first cut only removes the 1st contour including a part of the 2nd one. The second cutting pass removes material from the 2nd and 3rd contours, and the third cutting pass removes material from the 3rd contour and the filling one. The fourth cutting pass removes material created with the filling contour. As the scanning strategy differs between the outer (periphery) and inner (core) contours, hardness profile measurements were carried out from the periphery towards the center to investigate if there are any hardness gradients. The hardness was 225 ± 13 HK0.05 and 185 ± 19 HK0.05 for the PBF-LB and PBF-EB specimens, respectively. Comparable bulk hardness value, ~173 ± 9 HV1, was obtained in Ref. [18] using similar chemical composition and printing strategy for the PBF-EB technology. Moreover, no significant hardness variation was found between Top and Bottom and between the sample periphery and the core.

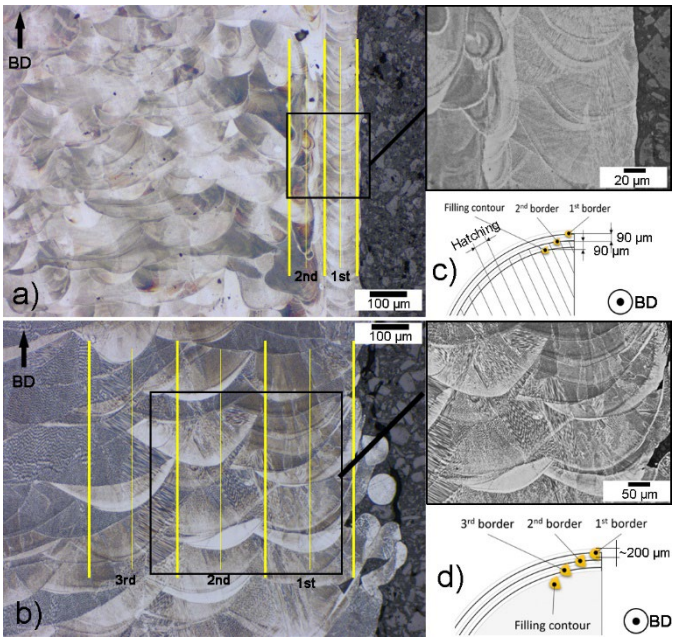

Fig. 2. Light optical micrographs showing the microstructure from the PBF-LB (a) and PBF-EB (b) samples. (c) – (d) illustrate the approximate thickness of the outer contours for the studied processes.

One possible explanation for the absence of a surface hardness increase in the as-printed samples is the use of different contour strategies, where the re-melting of the surface region would retain the heat causing a softening effect. For example, when annealing the 316L material in protective atmosphere at 1073K for 6 min, the microhardness will decrease from about 3.2 ± 0.1 GPa to about 2.2 ± 0.1 GPa [19]. Therefore, the hardness values obtained here show that the iterative heat cycling caused by successive multiple contour scanning led to a local softening of the sample surface layers. Also, due to the randomized texture without a predominant grain orientation, the re-melting process in the outer contour region will lower the near surface hardness [20]. The significantly lower hardness for the PBF-EB samples in comparison to the PBF-LB specimens can be explained by the greater segregation of Mo at the grain boundaries and the greater volume fraction of the formed nano-sized precipitates in the PBF-LB process [21, 22]. In addition, the larger grains as obtained with the PBF-EB compared to the PBF-LB is another mechanism that should further reduce the hardness. Fig. 3 provide the microhardness profiles of the samples after machining. For both processes, after the first (CL50) and final (CL20) cutting pass at the lowest cutting speed (V_c-130 m/min), the near-surface hardness increased to ~350 HV0.01 and ~450 HV0.01, respectively. This indicates the extensive work hardening that takes place in the material during the cutting process. As can be seen from the profile in Fig. 3a, the PBF-LB hardness values only reach the bulk ones after 50-µm depth, whereas in the case of PBF-EB, the hardness reaches the bulk value after 100-120 µm, indicating the main difference in the machining-affected depth. At V_c of 180 m/min, independent of the number of passes (CL50 through CL20), the PBF-LB produced samples obtained higher surface hardness as compared to the samples produced by PBF-EB. This contradicts the general notion that larger grains should facilitate dislocation movement and therefore lead to a higher degree of work hardening. In terms of affected volume (observation of

deformation bands) beneath the machined surfaces, we measured depths comparable to those observed for the surfaces machined at 130 m/min. When increasing V_c to 230 m/min, the PBF-LB samples behaved similarly to the samples produced at lower V_c, but with slightly lower degree of work hardening (lower hardness values). However, in the case of PBF-EB, a significantly different hardness profile was obtained, indicating significant work hardening already after the first cutting pass. As shown in Fig. 3c, the affected depth after machining was as large as 600 µm, which can be compared to about 100 µm at the lower cutting speeds and with 50 µm for the PBF-LB sample at the same speed. Comparable work hardening response as found here, for PBF-LB, was reported in Ref. [12]. However, a_p of 0.4 mm was used, where already with the first cutting pass they removed almost equal amount of material created with the contour and fill printing strategy, which might have an influence on the work hardening.

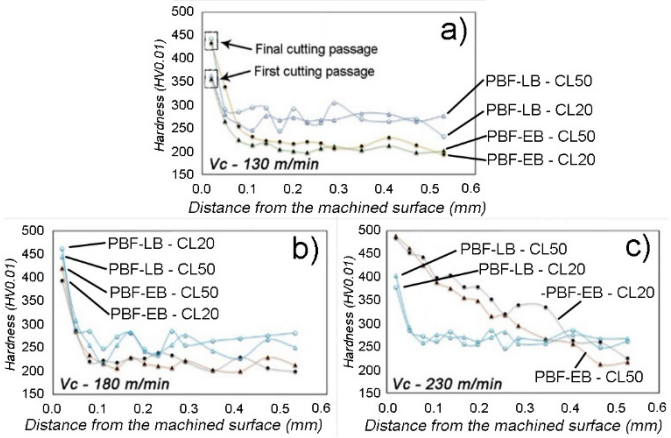

Fig. 3. (a) Micro-hardness profiles measured at the Top side of the test specimens after machining (b) 130 m/min, (c) 180 m/min, and (d) 230 m/min.

Fig. 4 show the near-surface cross-section images of the machined, polished, and etched surfaces. As can be seen in Fig. 4a-c, all surfaces show the presence of deformation bands. It should be noted that PBF-EB samples machined at 230 m/min have the deformation bands of up to ~500 µm beneath the machined surfaces. On the other hand, when machining at the lower cutting speeds, deformation bands reaches of up to ~100 µm. Such deformation bands were not observed for any of the cutting speeds when machining the PBF-LB samples. Despite the large region with deformation bands no white layers (nanocrystalline microstructure) were found at the machined surfaces of PBF-EB samples (see Fig. 5). Comparable observation of deformation bands was reported in Ref. [23] after studying the surface integrity and fatigue behavior of electric discharge machined and milled austenitic steels. The authors reported that the surface after machining was comprised of a severe plastic deformed region (white layer), heavily deformed region with nano-sized grains, and an affected region. The heavily deformed region was found to contain predominantly mechanical twins formed due to the severe shear forces induced by machining. This can be compared to the bended mechanical twins formed in a stress field generated in dynamic shear bands, which is the result of the steep strain gradient [24]. The results of the present study show that 316L made with two different AM-technologies shows very different work hardening behavior during machining. It is known that austenitic steels deform by three main mechanisms: dislocation slip, mechanical twinning, and martensite transformation. These mechanisms can act simultaneously or individually depending on the texture and the stacking fault energy (SFE) of the material. Considering the different microstructures in PBF-LB and PBF-EB, i.e. the melt pools and cooling rates, the cell structures, and the preferred orientation, the chip formation mechanism and newly generated surfaces will be affected.

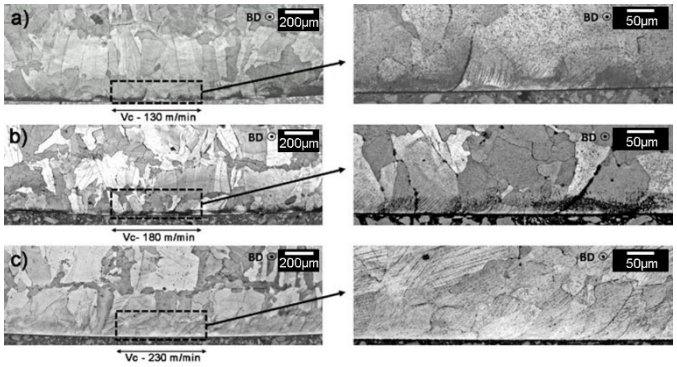

Fig. 4. Light optical micrographs showing the deformation bands for PBF-EB specimens after final cutting pass. (a) V_c- 130 m/min, (b) V_c – 180 m/min and (c) V_c – 230 m/min.

The influence of melt pool lines and internal pores on chip formation mechanisms and generated surfaces has been previously discussed in Ref. [25] when investigating the effects of cutting parameters on surface roughness and residual stresses of maraging steel produced by PBF-LB.

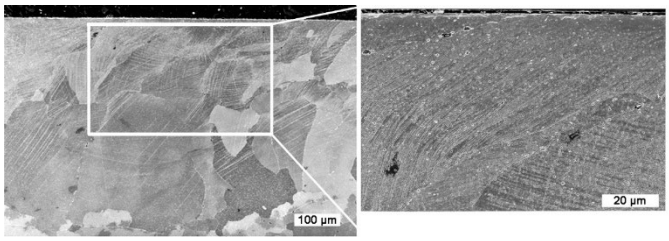

Fig. 5. Scanning electron micrograph showing the observed deformation bands in the PBF-EB specimen for CL20 machined at 230 m/min.

3.2 Effect of machining on surface topography and residual stresses

The average surface roughness, Sa, in the as-printed condition is 6 µm and 41 µm for PBF-LB and PBF-EB, respectively. When viewing along the length of the printed sample (in Z-direction), it is obvious that the surface is comprised of melted powder particles and irregular and distorted features formed due to layer-wise manufacturing. The corresponding topography, arithmetic mean height (Sa), and the ten-point height values (S10z) are shown in Fig. 6. The alternating surface roughness in the Z-direction as well as on the top of the specimens from the PBF processes is well known. Comparable surfaces roughness as observed here was reported in Ref. [12], who also confirmed that the traces of the laser scanning paths, where the melted powder particles appear to be concentrated to the boundaries of these traces. For the PBF-LB specimens, already after the first cutting pass the Sa- and S10z-values are significantly improved, and only minor changes are noted for CL20. The Sa-value is ~1.5 µm, and the S10z-values are between 5 and 10 µm. For the PBF-EB, the CL50 resulted

in a Sa value of ~1 µm for the two higher cutting speeds (180 m/min and 230 m/min), while at 130 m/min, the Sa was measured to be ~3 µm. For CL20, the higher cutting speeds resulted in a Sa of ~2 µm, and the 130 m/min resulted in a Sa of ~4 µm. Hence, in the case of the PBF-LB specimens no changes were recorded between CL50 and CL20, whereas the PBF-EB clearly showed an increase in the surface roughness with increased engagement time. The results show clear differences in the obtained surface topography for the PBF-LB and PBF-EB specimens. For the PBF-LB, a good surface finish can be achieved after just one cut and is almost unaffected after the final cut. Whereas for the PBF-EB the first cut is resulting in the best surface topography and tends to get deteriorated with increase in cutting passes.

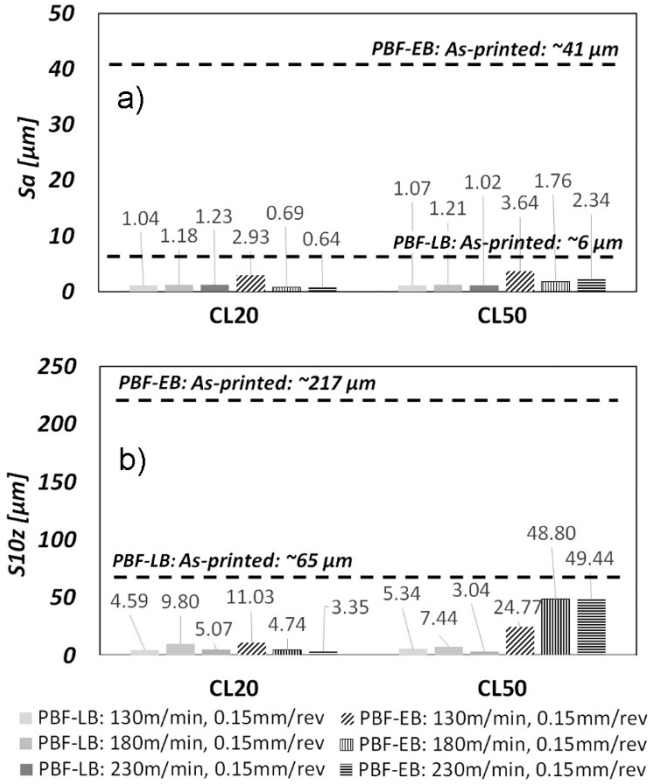

Fig. 6. Surface topography parameters for the L-BPF and PBF-EB samples, a) arithmetic mean height (Sa) and b) ten point height (S10z) values calculated according to ISO 25178-2:2012.

Concerning the stresses, the PBF-LB samples showed tensile residual stresses in the as-printed condition (570 MPa in the building direction and 300 MPa in the transverse direction). This can be compared to the beneficial compressive residual stresses that was measured for the PBF-EB samples (independent of the building direction). The compressive stresses were in the order of ~150 MPa in the building direction and ~60 MPa across the building direction for the PBF-EB specimens. After machining, the residual stress profiles are characterized by tensile stresses at the surface, which shifts to compressive residual stresses at ~30 µm depth and thereafter increasing slightly with depth. The hook-shaped stress profile is typically observed in turning and has a beneficial effect on the fatigue life [26]. For PBF-LB, only minor changes were observed between the different cutting speeds and cutting passes. For the PBF-EB, 130 m/min and 180 m/min, did not show any conclusive reducing trends for the tensile residual stresses values for increasing cutting speed. Only at 230 /min, the surface and subsurface residual stresses were shifted towards less tensile- (cutting direction) and higher compressive- (feed direction) residual stresses. The PBF-EB specimens have higher surface tensile stresses at the two lower cutting speeds as compared to the PBF-LB specimens. A higher cutting speed will create a higher temperature, which will soften the material and thus allowing for a higher degree of strain hardening. Austenitic stainless steels are known to be difficult to machine materials due to their low thermal conductivity and high sensitivity to strain / stress rate and work hardening. Relatively low thermal conductivity of the material leads to heat concentration at the cutting edge, resulting in strongly localized high temperature zone, which in turn softens the material during cutting. The results show that the different microstructures will have an influence on the final surface integrity (magnitude and profile of the stresses). Furthermore, we observed that the residual stresses do not change significantly with each cutting pass, which in part might be connected to the relationship between the a_p and the thickness of the contours. However, by optimizing the machining process, it is possible to tune the residual stresses to obtain beneficial compressive stresses.

With respect to tool wear, for each machining condition, the cutting tools were analyzed after the completion of individual cutting steps. No significant tool wear was observed for all studied samples and cutting conditions. Notably, the total spiral cut length is only ~239 m. Table 2 summarizes the measured maximum V_{B_max} at various cutting speeds. As expected, irrespective of the machined material the highest flank wear was found for V_c 230 m/min. The cutting tools used when machining the low hardness PBF-EB specimens showed slightly higher flank wear compared to the tools used to machine the PBF-LB specimens, which is in line with the observed surface topography (increased tool wear for rougher surfaces). It is well known that knowledge of hardness and grain size are not enough to understand or predict the tool wear when machining conventional 316L SS [27]. Hence, a dedicated tool wear study with detailed characterization of as-printed material (grain size distribution, micro constituents, crystallographic orientation, Kernel average misorientation etc.) is needed to fully understand the wear progression and behavior when machining additively manufactured 316L SS. Adhesion of work piece material on the rake side was also observed irrespective of the samples.

Table 2. Measured tool flank wear, V_{B_max}, for the studied cutting speeds and manufacturing processes, PBF-LB and PBF-EB.

Material / Speed	130 m/min	180 m/min	230 m/min
PBF-LB	< 0.01 mm	< 0.01 mm	< 0.01 mm
PBF-EB	<0.02 mm	0.02 mm	0.03 mm

4. Conclusions

The effect of machining on the integrity of 316L austenitic stainless steel produced by PBF-LB and PBF-EB was studied. The surface integrity of the as-machined surfaces was investigated with respect to cutting forces, tool wear, surface topography, residual stresses, surface deformation, and hardness. The following conclusions are drawn:

- Once the near surface material printed with the contour strategy was removed, comparable surface topography was obtained for both the studied processes, PBF-LB and PBF-EB.
- The hardness profiles revealed that work hardening takes place in the materials produced by both PBF-LB and PBF-EB. The hardness increased between 2- 2.5 times, reaching ~400 HV0.1 for PBF-LB and ~500 HV0.1 for PBF-EB after machining. Hence, more work hardening took place in PBF-EB, which was in line with the observed deformation bands near the machined surfaces.
- The residual stresses in the as-printed condition was characterized by high surface and subsurface tensile residual stresses for the PBF-LB specimens, while the PBF-EB specimens were characterized by mainly compressive residual stresses. After machining, the surfaces stresses were first tensile and then compressive and reached a minimum at a depth of about 30 µm below the surface.
- Independent on the studied cutting speed, no tool flank wear could be seen when machining the PBF-LB specimens, whereas for the PBF-EB specimens, machining at 130 m/min and 180 m/min resulted in V_{B_max} 0.02 mm. For the highest cutting speed, 230 m/min, V_{B_max} 0.03 mm was measured.

Acknowledgement

Amir-Reza Shahab is acknowledged for initial work. This study is a collaboration between RISE AB, the Centre for Metal Cutting Research and the Centre for Additive Manufacture – Metal at Chalmers University of Technology, and Mid Sweden University. We thank Swedish Governmental Agency of Innovation Systems (Vinnova 2016-05175) for funding. Rolf Ahlman at RISE AB and Dr. Sinuhe at Sandvik Coromant are thanked for their support with turning tests and providing the respective machining tools.

References

[1] T. DebRoy, H.L. Wei, J.S. Zuback, T. Mukherjee, J.W. Elmer, J.O. Milewski, A.M. Beese, A. Wilson-Heid, A. De, W. Zhang, Additive manufacturing of metallic components – Process, structure and properties, Prog. Mater Sci. 92 (2018) 112–224.

[2] Z. Liu, B. He, T. Lyu, Y. Zou, A Review on Additive Manufacturing of Titanium Alloys for Aerospace Applications: Directed Energy Deposition and Beyond Ti-6Al- 4V, JOM 73 (2021) 1804–1818.

[3] A.M. Vilardell, S.B. Hosseini, M. Åsberg, A. Dahl-Jendelin, P. Krakhmalev, C. Oikonomou, S. Hatami, Evaluation of post-treatments of novel hot-work tool steel manufactured by laser powder bed fusion for aluminum die casting applications, Mater Sci Eng 800 (2021)

[4] C. Sun, Y. Wang, M.D. McMurtrey, N.D. Jerred, F. Liou, J. Li, Additive manufacturing for energy: A review, Applied Energy 282 (A) (2021) 116041. https://doi.org/10.1016/j.apenergy.2020.116041.

[5] L.E. Murr, S.M. Gaytan, D.A. Ramirez, E. Martinez, J. Hernandez, K.N. Amato, P.W. Shindo, F.R. Medina, R.B. Wicker, Metal fabrication by additive manufacturing using laser and electron beam melting technologies, J Mater Sci Technol 28 (1) (2012) 1-14.

[6] Y. Zhong, L.-E. Rännar, L. Liu, A. Koptyug, S. Wikman, J. Olsen, D. Cui, Z. Shen, Additive manufacturing of 316L stainless steel by electron beam melting for nuclear fusion applications, Journal of Nuclear Materials 486 (2017) 234-245.

[7] S. Hatami, T. Ma, T. Vuoristo, J. Bertilsson, O. Lyckfeldt, Fatigue Strength of 316 L Stainless Steel Manufactured by Selective Laser Melting, JMEPEG 29 (2020) 3183–3194.

[8] W.E. Frazer, Metal Additive Manufacturing: A Review. J. of Materi Eng and Perform 23, (2014) 1917-1928.

[9] D. Wang, Y. Liu, Y. Yang, Theoretical and experimental study on surface roughness of 316L stainless steel metal parts obtained through selective laser melting, Rapid Prototyping Journal 22/4 (2016)706-716

[10] B. Vayssette, N. Saintier, C. Brugger, M. El-May, E. Pessard, Surface roughness of Ti-6Al-4V parts obtained by SLM and EBM: Effect on the High Cycle Fatigue life, Procedia Engineering, Elsevier, 2018, 213, pp.89-97

[11] T. Pasang, B. Tavlovich, O. Yannay, B. Jackson, M. Fry, Y. Tao, C. Turangi, J.-C. Wang, C.-P. Jiang, Y. Sato, M. Tsukamoto, W.Z. Misiolek, Directionally-Dependent Mechanical Properties of Ti6Al4VManufactured by Electron Beam Melting (EBM) and Selective Laser Melting (SLM), Materials 2021, 14, 3603.

[12] Y. Kaynak, O. Kitay, The effect of post-processing operations on surface characteristics of 316L stainless steel produced by selective laser melting, Additive Manufacturing 26 (2019) 84-93.

[13] A. Y. Al-Maharma1, S. P. Patil, B. Markert, Effects of porosity on the mechanical properties of additively manufactured components: a critical review, Mater. Res. Express 7, (2020), 122001,

[14] D. Mallipeddi, T. Hajali, L-E. Rännar, A. Bergström, S. Hernandez, E. Strandh, L. Nyborg, P. Krajnik, Surface Integrity of Machined Electron Beam Melted Ti6Al4V Alloy Manufactured with Different Contour Settings and Heat Treatment, Procedia CIRP, Volume 87, 2020, Pp. 327-332

[15] European Commitee for Standardization. EN 15305:2008, Non-Destructive Testing – Test Method for Residual Stress Analysis by X-ray Diffraction 2008; European Commitee for Standardization: Brussels, Belgium, 2008

[16] ISO 4287:1997 Geometrical Product Specifications (GPS)–Surface texture: Profile method–Terms, definitions and surface textures parameters (Geneva: International Organizations for Standardization).

[17] ISO 25178-2:2012 Geometrical product specifications (DPS)–Surface texture: Areal – Part 2: Terms, definitions and surface texture parameters (Geneva: Internationals Organizations for Standardization).

[18] L.-E. Rännar, A. Koptyug, J. Olsén, K. Saeidi, Z. Shen, Hierarchical structures of stainless steel 316L manufactured by Electron Beam Melting, Additive Manufacturing 17 (2017) 106–112.

[19] K. Saeidi, X. Gao, Y. Zhong, Z.J. Shen, Hardened austenite steel with columnar sub- grain structure formed by laser melting. Mater Sci Eng A 625 (2015) 221–229.

[20] B. Mehta, E. Hryha, L. Nyborg, F. Tholence, E. Johansson, Effect of Surface Sandblasting and Turning on Compressive Strength of Thin 316L Stainless Steel Shells Produced by Laser Powder Bed Fusion. Metal 11 (2021) 1070

[21] N.L. Liu, Q. Ding, Y. Zhong, J. Zou, J. Wu, Y.L. Chiu, J. Li, Z. Zhang, Q. Yu, Z. Shen, Dislocation network in additive manufactured steel breaks strength-ductility tradeoff, Mater Today 21 2017, 354-361

[22] S.-H.H. Kim, H. Kim, N.J. Kim, Brittle intermetallic compound makes ultra-strong low-density steel with large ductility, Nature 518 2015 77-79

[23] M. Lundberg, J. Saarimäki, J. Moverare, M. Calmunger, Surface Integrity and Fatigue Behaviour of Electric Discharged Machined and Milled Austenitic Stainless Steel, Materials Characterization 124 (2017) 215-222

[24] Q. Xue, J.F. Bingert, B.L. Henrie, G.T. Gray III, EBSD characterization of dynamic shear band regions in pre-shocked and as-received 304 stainless steels, Mater Sci Eng A 473 (2008) 279-289.

[25] S. Afkhami, M. Dabiri, H. Piili, T. Björk, Effects of manufacturing parameters and mechanical post-processing on stainless steel 316L processed by laser powder bed fusion, Mater Sci Eng A 802 (2021) 140660

[26] N. Jouini, P. Revel, G. Thoquenne, Influence of Surface Integrity on Fatigue Life of Bearing Rings Finished by Precision Hard Turning and Grinding, Journal of Manufacturing Processes, 57 (2020), pp. 444-451

[27] P. Hoier, A. Malakizadi, S. Friebe, U. Klement, P. Krajnik, Microstructural variations in 316L austenitic stainless steel and their influence on tool wear in machining Wear Vol.428-429 (2019) 315-327